Supporting Information

Unlocking high absorption efficiency of Cr^{3+} ions in magnesium titanates with intrinsically high octahedron distortion

*Shijie Yu, Longfei Li, Jie Zhang, Yixin Sun, Leqi Yao, Chao Liang, Jinhua He, Jianqing Jiang, and Qiyue Shao**

S. Yu, L. Li, J. Zhang, Y. Sun, Q. Shao

School of Materials Science and Engineering

Southeast University

Nanjing 211189, China

E-mail: qiyueshao@seu.edu.cn

L. Yao, C. Liang, J. He

Jiangsu Bree Optronics Co., Ltd.

Nanjing 211103, China

J. Jiang

College of Mechatronics Engineering

Nanjing Forestry University

Nanjing 210037, China

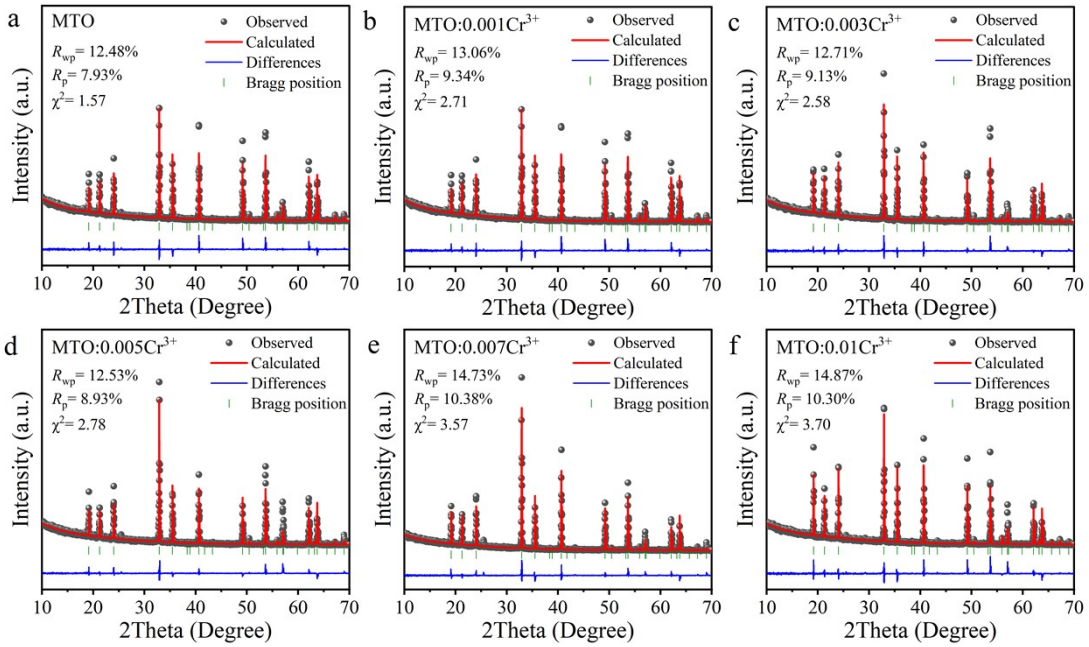

Figure S1. Refined XRD patterns of the a) MTO, b) MTO:0.001Cr^{3+}, c) MTO:0.003Cr^{3+}, d) MTO:0.005Cr^{3+}, e) MTO:0.007Cr^{3+}, and d) MTO:0.01Cr^{3+} samples.

Table S1 The refined structural parameters of MTO:mCr^{3+} (m = 0, 0.001, 0.003, 0.005, 0.007, 0.01).

m	**0**	**0.001**	**0.003**	**0.005**	**0.007**	**0.01**
Crystal system	Trigonal					
Space group	$R\bar{3}$					
$a = b$ (Å)	5.05516	5.05499	5.05473	5.05465	5.05459	5.05444
c (Å)	13.89770	13.89775	13.89720	13.89720	13.89675	13.89567
α = β (°)	90					
γ (°)	120					
Z	6					
V (Å^3)	307.5696	307.5500	307.5062	307.4955	307.4792	307.43706
R_p	7.93%	9.34%	9.13%	8.93%	10.38%	10.30%
R_{wp}	12.48%	13.06%	12.71%	12.53%	14.73%	14.87%
χ^2	1.57	2.71	2.58	2.78	3.57	3.70

Table S2 The atomic positions, thermal vibration parameters, and site occupancies by utilizing Rietveld refinement for the representative MTO:0.005Cr^{3+}.

	Atom	x	y	z	Occ.	Uiso
1	O	0.31433	0.02435	0.24699	1	0.01776
2	Mg	0	0	0.35470	0.9975	0.01668
3	Ti	0	0	0.14533	0.9975	0.01011
4	Cr_{Mg}	0	0	0.35470	0.0025	0.01174
5	Cr_{Ti}	0	0	0.14533	0.0025	0.00643

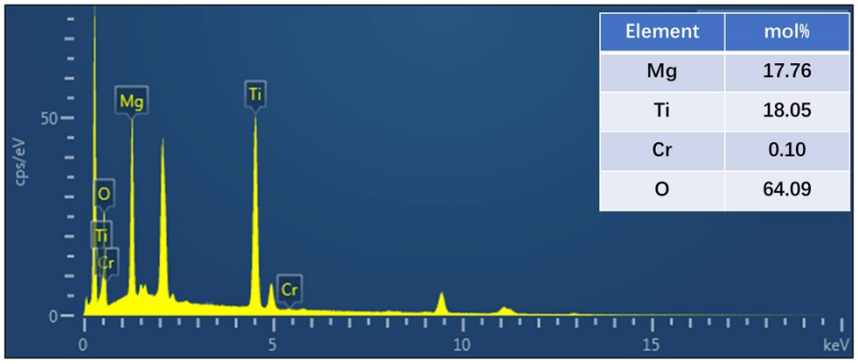

Figure S2. EDS spectrum of MTO:0.005Cr^{3+} and molar contents of constituent elements.

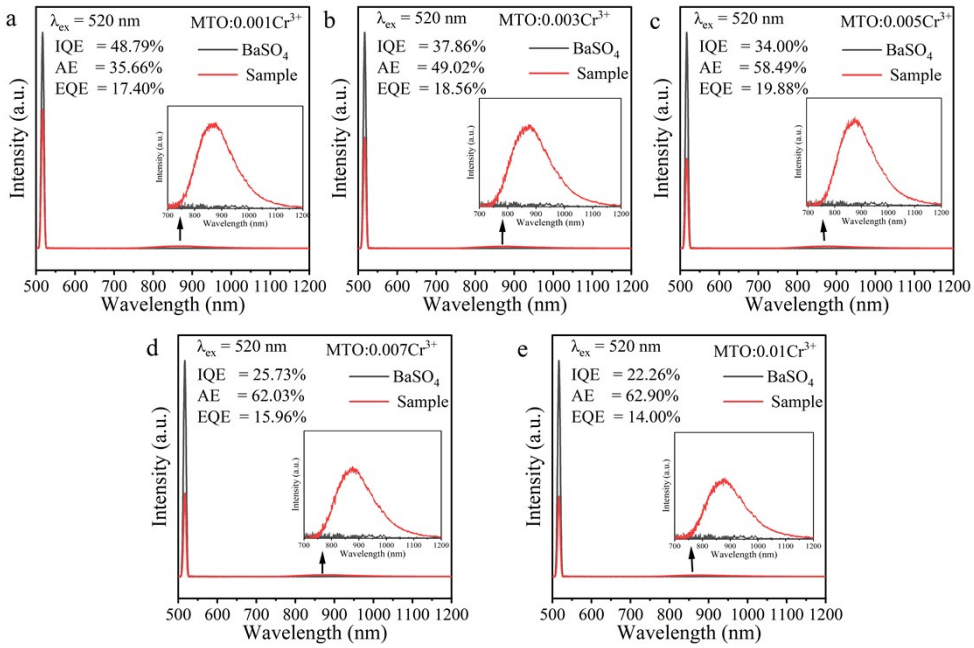

Figure S3. Quantum efficiency (QE) measuring spectra of MTO:*m*Cr^{3+} phosphors: a) *m*=0.001, b) *m*=0.003, c) *m*=0.005, d) *m*=0.007, e) *m*=0.01.

Table S3 Bond angles and bond angle variance σ^2 of $[MgO_6]$ and $[TiO_6]$ octahedra in MTO:0.005Cr^{3+}.

Polyhedron	Angle ∠ Mg-O-Mg	Angle ∠ Ti-O-Ti	bond angle variance (σ^2)
$[MgO_6]$	99.3007° × 3 92.3093° × 3 89.3282° × 3 77.0040° × 3		71.2318
$[TiO_6]$		104.1816° × 3 89.6993° × 3 83.0706° × 3 81.0030° × 3	90.0466

The bond angle variance σ^2 are defined according the following equation:[1]

$$\sigma^2 = \sum_{i=1}^{12} \left| \frac{(\theta_i - \theta_0)^2}{11} \right| \quad \text{(S1)}$$

Where θ_0 is the ideal bond angle (90°) for a regular octahedron, and θ_i is the ith bond angle. On the basis of the refined results of XRD patterns. The calculated bond angle variance σ^2 for $MgTiO_3$ is significantly higher than that in $InBO_3$ (σ^2 = 3.4342) and $Na_{1.4}Al_{0.3}Ti_{1.6}(PO_4)_3$ (σ^2 = 15.7190),[1,2] which indicates there is substantial angular bending in $MgTiO_3$ system.

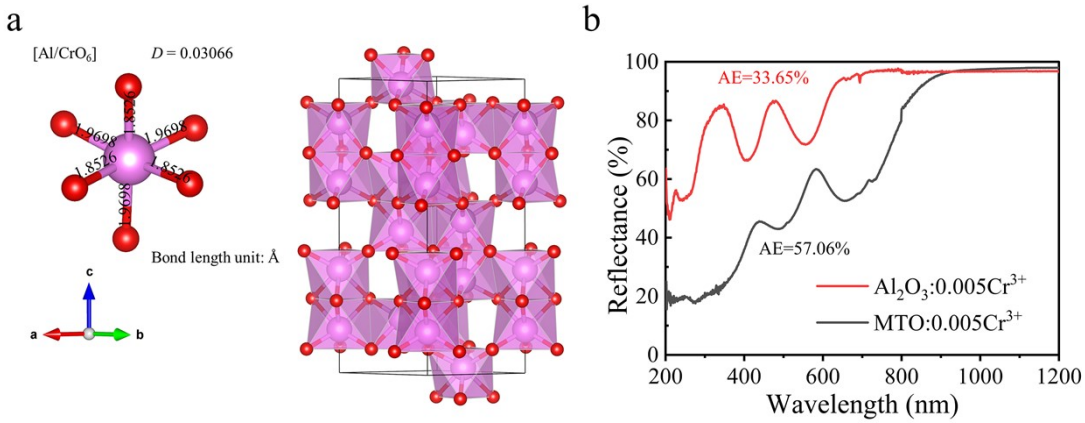

Figure S4. a) Crystal structure of Al_2O_3 (inset shows bond lengths and distortion index *D* of $[AlO_6]$); b) DR spectra of MTO:0.005Cr^{3+} and Al_2O_3:0.005Cr^{3+}.

Al_2O_3 shares a similar crystal structure with MTO and can be regarded as two Al atoms substituting for one Mg and one Ti, respectively. The calculated octahedral distortion index (*D*) for $[AlO_6]$ is 0.03066, which is smaller than the average *D* value of $[MgO_6]$ and $[TiO_6]$ in MTO. Under identical synthesis conditions as MTO:0.005Cr^{3+}, the Al_2O_3:0.005Cr^{3+} phosphor was prepared, and its absorption efficiency (AE) was determined to be 33.65% via DR spectroscopy, which is significantly lower than that of MTO:0.005Cr^{3+}. These results provide strengthened evidence for the proposed distortion-enabled absorption mechanism.

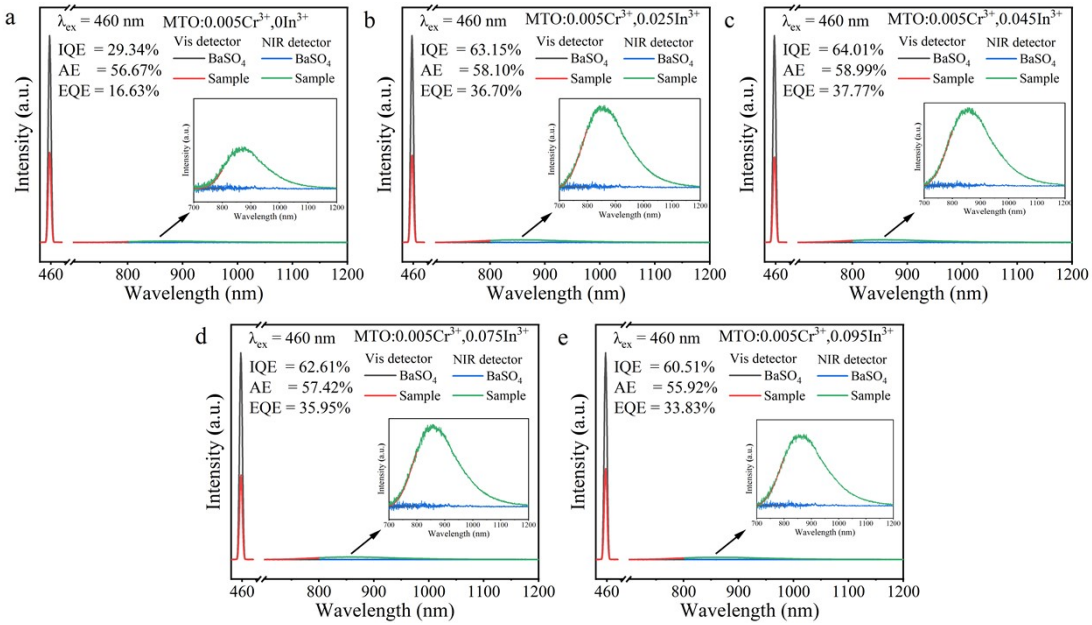

Figure S5. Quantum efficiency (QE) measuring spectra of MTO:0.005Cr^{3+},*n*In^{3+} phosphors: a) *n*=0, b) *n*=0.025, c) *n*=0.045, d) *n*=0.075, e) *n*=0.095.

The internal QE (IQE), external QE (EQE) and absorption efficiency (AE) are calculated using the following equations:[3]

$$IQE = \frac{\int L_S - \int L_R}{\int E_R - \int E_S} \times 100\% \quad \text{(S2)}$$

$$EQE = \frac{\int L_s}{\int E_R} \times 100\% \quad \text{(S3)}$$

$$AE = \frac{\int E_R - \int E_S}{\int E_R} \times 100\% \quad \text{(S4)}$$

Where L_S and L_R are the luminescent spectra of the sample and reference ($BaSO_4$), respectively. E_S and E_R are the excitation light spectra for the sample and reference, respectively. The FLS1000 spectrophotometer is equipped with two photodetectors, but both cannot respond accurately in a broad spectral range from the blue to NIR light. Therefore, the excitation spectra (E_S and E_R) were measured by the visible (VIS) detector, while the luminescent spectra (L_S and L_R) were measured by the NIR detector. The difference in sensitivity of the two detectors was carefully calibrated by successively measuring the luminescent spectra of the sample in the spectral range of 680–800 nm. Both VIS and NIR detectors can accurately respond in 680–800 nm. Accordingly, the luminescent spectrum LS is calibrated by the following equation:

$$L_S = \left(\int_{800}^{680} L_{VIS} / \int_{800}^{680} L_{NIR} \right) \times L_{NIR} \quad \text{(S5)}$$

where L_{VIS} and L_{NIR} represent the luminescent spectrum of the sample recorded by the VIS and NIR detector, respectively. After calibration, L_S, E_S and E_R can be obtained in the same response ability.

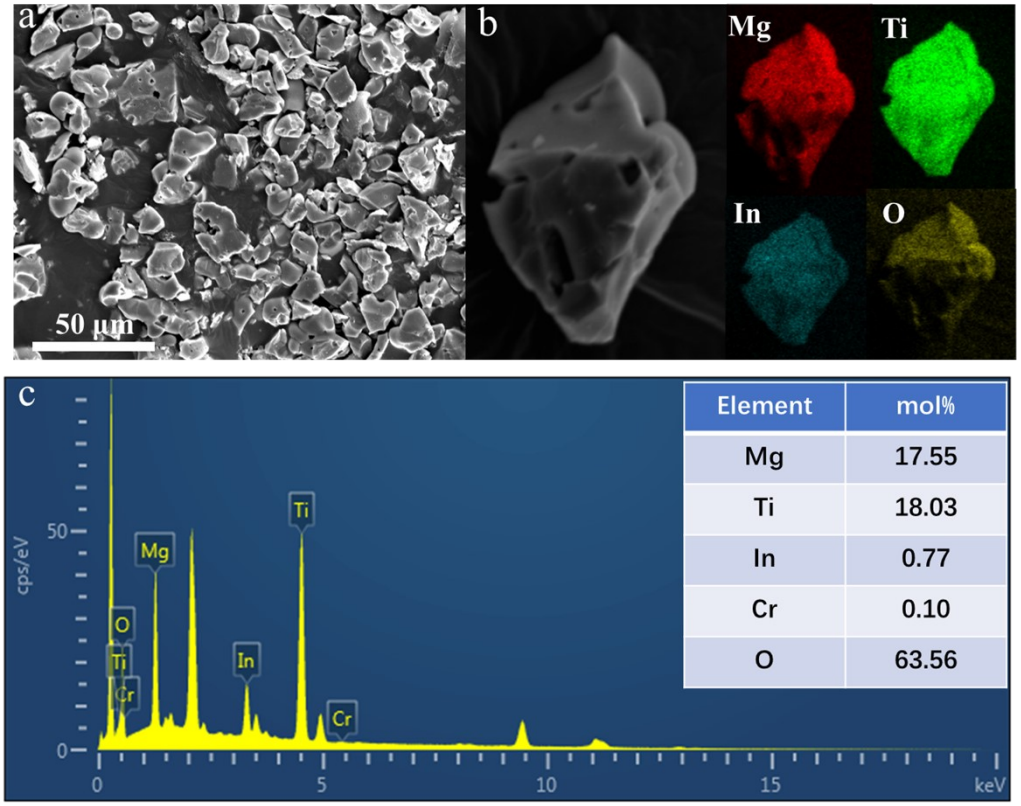

Figure S6. a) SEM image b) EDS elemental mapping images, and c) EDS spectrum and elemental quantitative data of MTO:0.005Cr^{3+},0.045In^{3+}.

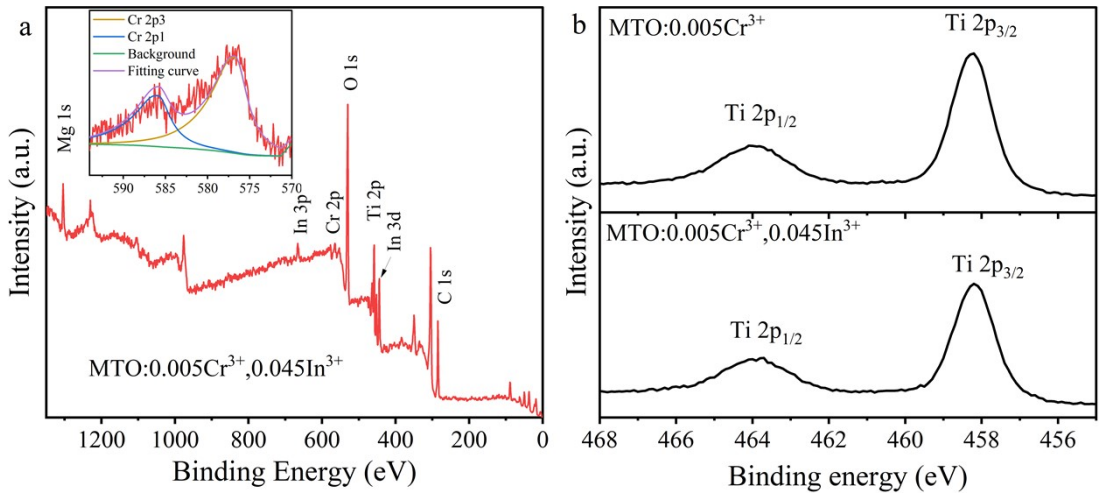

Figure S7. a) XPS curve of MTO:0.005Cr^{3+},0.045In^{3+}, the inset shows high-resolution Cr 2p spectrum. b) Ti 2p high resolution XPS spectra of MTO:0.005Cr^{3+} and MTO:0.005Cr^{3+},0.045In^{3+}.

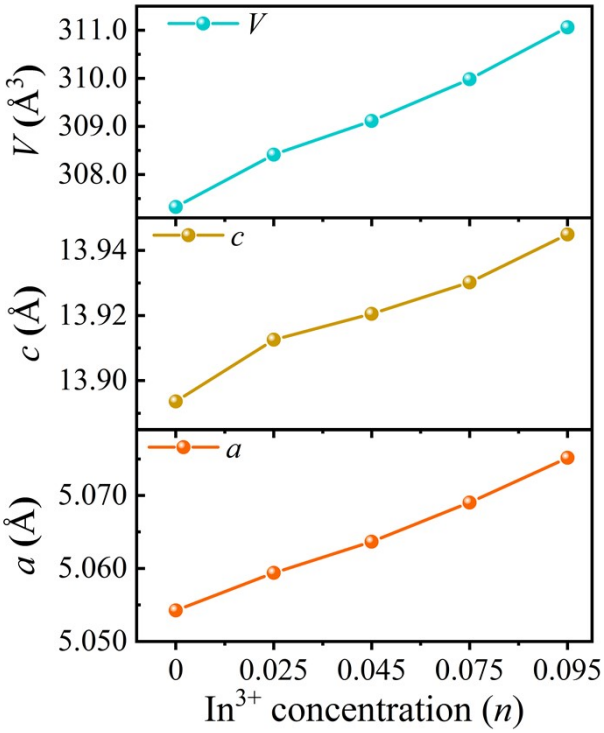

Figure S8. The refined lattice parameters (*a* and *c*) and unit-cell volume (*V*) of MTO:0.005Cr^{3+},*n*In^{3+} (*n* = 0, 0.025, 0.045, 0.075, 0.095).

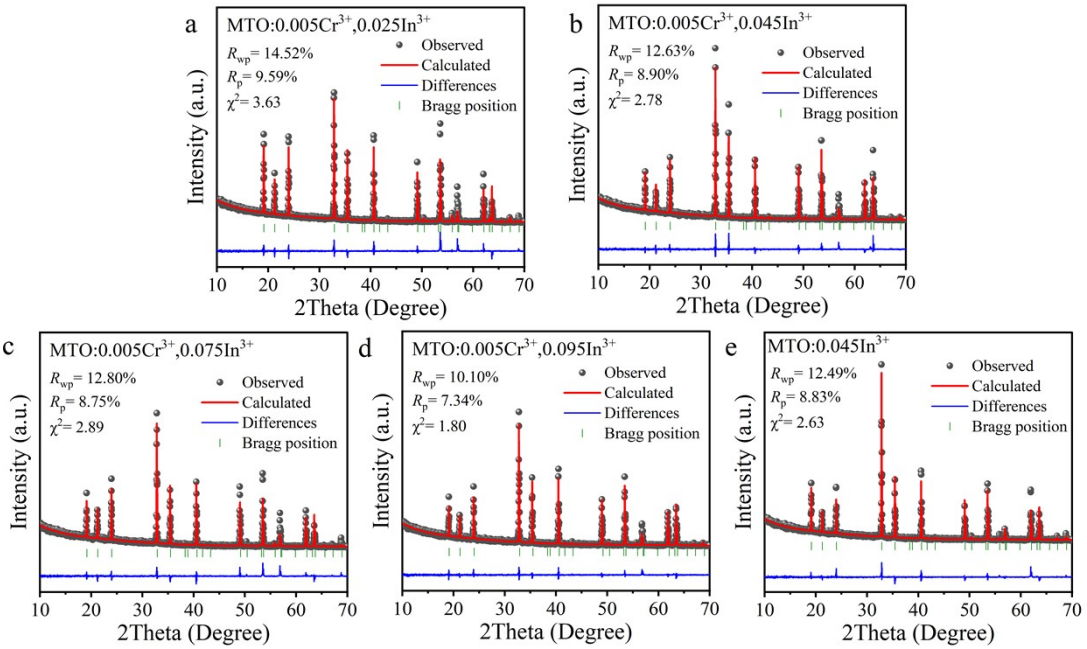

Figure S9. Refined XRD patterns of a) MTO:0.005Cr^{3+},0.025In^{3+}, b) MTO:0.005Cr^{3+}, 0.045In^{3+}, c) MTO:0.005Cr^{3+},0.075In^{3+}, d) MTO:0.005Cr^{3+},0.095In^{3+}, and e) MTO 0.045In^{3+}.

Table S4 Refined structural parameters of MTO:0.005Cr^{3+},*n*In^{3+} (*n* = 0, 0.025, 0.045, 0.075, 0.095) and MTO:0.045In^{3+}.

n	**0**	**0.025**	**0.045**	**0.075**	**0.095**	**MTO: 0.045In^{3+}**
Crystal system			Trigonal			Trigonal
Space group			$\bar{R}3$			$\bar{R}3$
a = *b* (Å)	5.05465	5.05939	5.06367	5.06903	5.07514	5.06379
c (Å)	13.89720	13.91256	13.92053	13.93016	13.94487	13.91796
α = β (°)			90			90
γ (°)			120			120
Z			6			6
V (Å^3)	307.4955	308.414	309.133	309.982	311.058	309.0705
R_p	8.93%	9.59%	8.90%	8.75%	7.34%	8.83%
R_{wp}	12.53%	14.52%	12.63%	12.80%	10.10%	12.49%
χ^2	2.78	3.63	2.78	2.89	1.80	2.63

Table S5 The atomic positions, thermal vibration parameters, and site occupancies by utilizing Rietveld refinement for the representative MTO:0.005Cr^{3+},0.045In^{3+}.

	Atom	x	y	z	Occ.	Uiso
1	O	0.32535	0.01892	0.24579	1	0.00486
2	Mg	0	0	0.35656	0.9750	0.00110
3	Ti	0	0	0.14648	0.9750	0.00534
4	Cr_{Ti}	0	0	0.14648	0.0050	0.17886
5	In_{Mg}	0	0	0.35656	0.0250	2.22917
6	In_{Ti}	0	0	0.14648	0.0200	2.98737

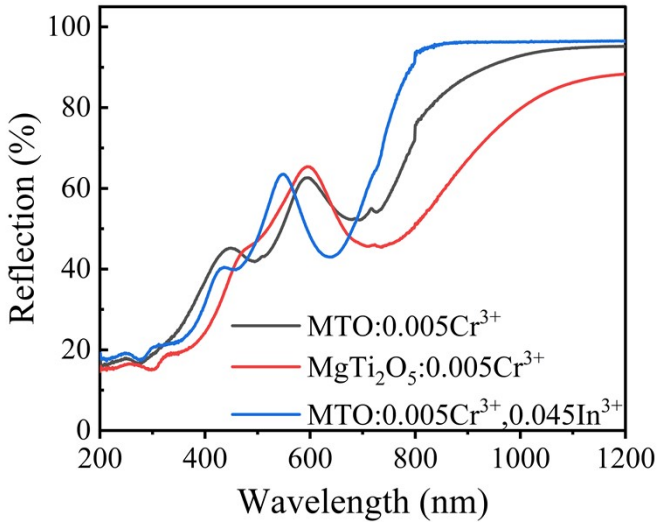

Figure S10. DR spectra of MTO:0.005Cr^{3+}, $MgTi_2O_5$:0.005Cr^{3+}, and MTO:0.005Cr^{3+},0.045In^{3+}.

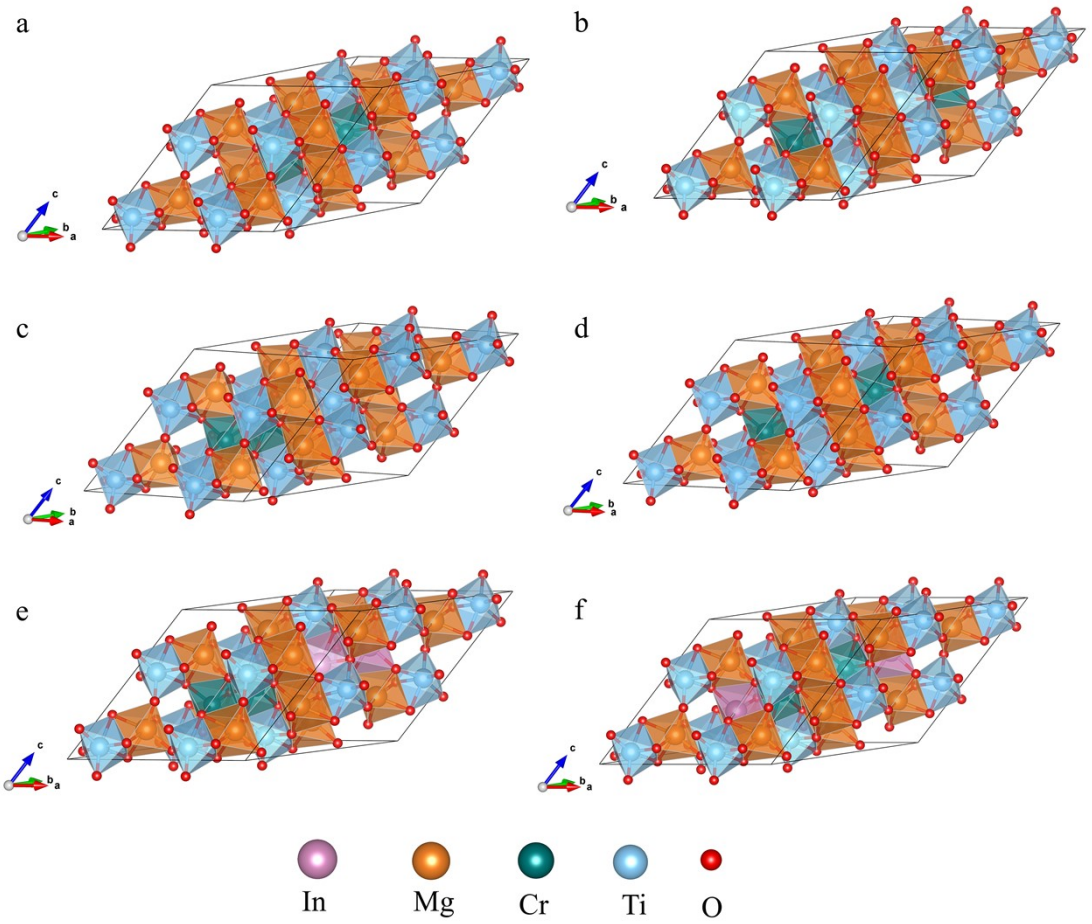

Figure S11. Crystal structure of $Mg_{16}Ti_{16}O_{48}$ with Cr^{3+} occupying different sites: a) Cr^{3+} exclusively occupying Ti^{4+} sites, b) Cr^{3+} exclusively occupying Mg^{2+} sites, c) two Cr^{3+} ions substituting for adjacent Mg^{2+} and Ti^{4+} sites (closely coupled), d) two Cr^{3+} ions substituting for Mg^{2+} and Ti^{4+} sites that are far apart, e) two Cr^{3+}/In^{3+} ions substituting for adjacent Mg^{2+} and Ti^{4+} sites, and f) In^{3+} and Cr^{3+} substituting for adjacent Mg^{2+} and Ti^{4+} sites respectively (Cr^{3+} ions well separated).

Table S6 Calculated formation energies (ΔE_f) of potential Cr^{3+} occupation situations in $Mg_{16}Ti_{16}O_{48}$.

Energy	MTO:Cr^{3+}				MTO:Cr^{3+},In^{3+}	
	Cr_{Ti}	Cr_{Mg}	Cr_{Mg}-Cr_{Ti} pair	Isolated Cr_{Mg}/Cr_{Ti}	Cr_{Mg}-Cr_{Ti} pair	In_{Mg}-Cr_{Ti}
E(doped)	-615.35	-629.74	-623.66	-623.32	-611.75	-612.36
E(pure)	-619.51	-619.51	-619.51	-619.51	-619.51	-619.51
μ(Mg)		-1.54	-1.54	-1.54	-1.54	-1.54
μ(Ti)	-7.76		-7.76	-7.76	-7.76	-7.76
μ(In)					-2.55	-2.55
μ(Cr)	-9.51	-9.51	-9.51	-9.51	-9.51	-9.51
ΔE_f	7.66	5.71	5.57	5.91	13.28	12.67

The forming energy was calculated using the following formula:[4]

$$\Delta E_{form} = \mathrm{E}\,(doped) - \mathrm{E}\,(pure) + q\sum n_x \mu_x \quad \text{(S6)}$$

Where E(doped) is the total energy of the doped system, E(pure) is the total energy of the undoped system, and μ_x is the chemical potential of the defect element x and n_x is the number of elements removed (q = +1) or doped (q = -1) during the formation of defect structure.

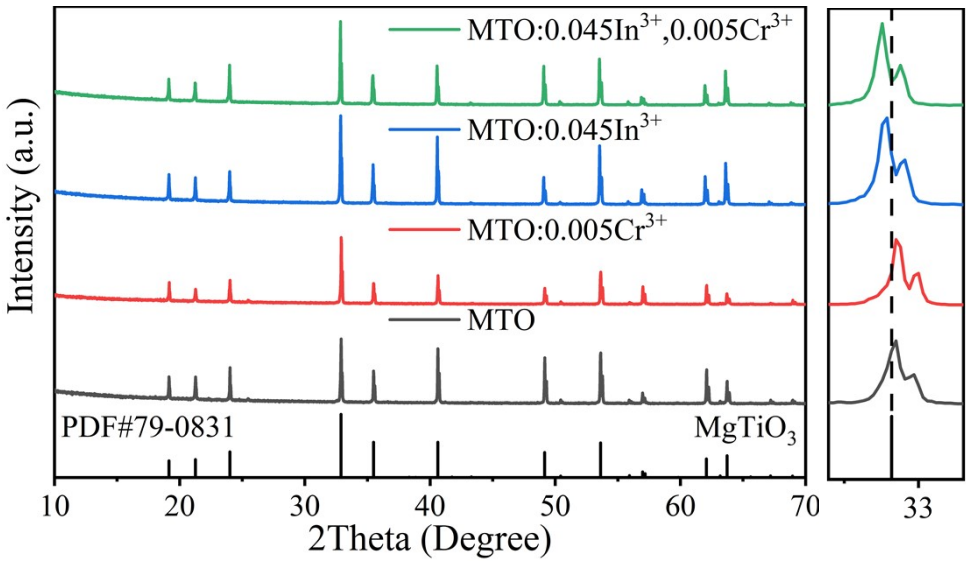

Figure S12. Comparison of XRD diffraction patterns of MTO/MTO:0.005Cr^{3+} with and without In^{3+} doping.

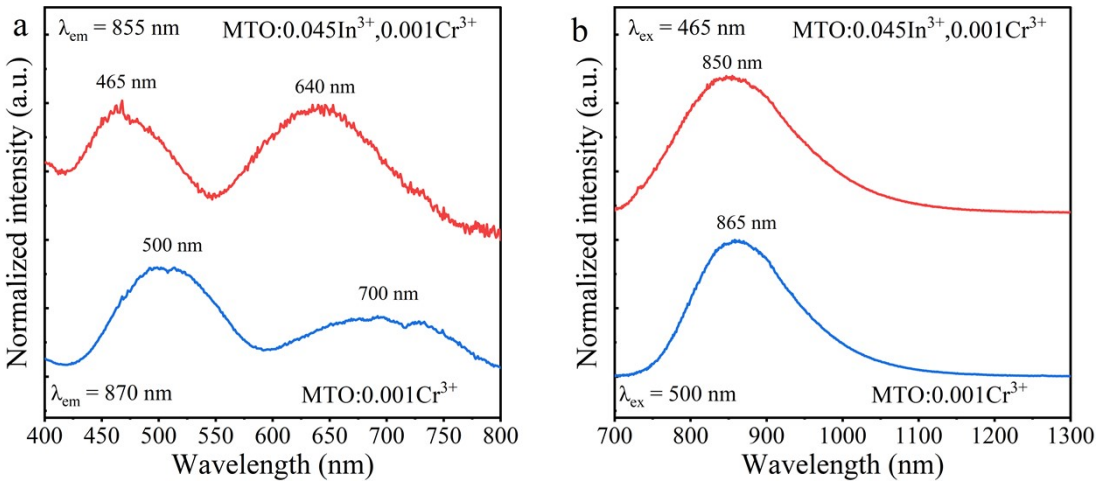

Figure S13. a) PLE of MTO:0.001Cr^{3+} and MTO:0.045In^{3+},0.001Cr^{3+}. b) PL of MTO:0.001Cr^{3+} and MTO:0.045In^{3+},0.001Cr^{3+}.

Table S7 Luminescent parameters of Cr^{3+} in MTO:0.001Cr^{3+} and MTO:0.045In^{3+},0.001Cr^{3+}.

Phosphor	λ_{ex} (nm)	λ_{em} (nm)	$E(^4T_2)$ (cm^{-1})	ΔS (cm^{-1})	Dq (cm^{-1})	B $(cm^{-1})_i$	Dq/B
MTO: 0.001Cr^{3+}	500 700	865	5714.29	2725.02	1292.32	593.88	2.176
MTO: 0.045In^{3+}, 0.001Cr^{3+}	465 640	850	5880.38	3860.29	1369.49	603.58	2.269

$E(^4T_2)$, ΔS, Dq and B represent the energy position of $^4T_2$, Stokes shift, crystal field strength parameter and Racah parameter, respectively. The crystal field strength parameter Dq and Racah parameter B are calculated using the following equations:[1]

$$10D_q = E\left(^4A_2 \rightarrow {}^4T_2\right) \tag{S7}$$

$$\frac{D_q}{B} = \frac{15\left(\frac{x}{Dq} - 8\right)}{(x/Dq)^2 - 10(x/Dq)} \tag{S8}$$

$$x = E\left(^4T_1\right) - E\left(^4T_2\right) = E\left(^4A_2 \rightarrow {}^4T_1\right) - E\left(^4A_2 \rightarrow {}^4T_2\right) \tag{S9}$$

Where $E\left(^4T_1\right)$ and $E\left(^4T_2\right)$ are the energy position of the $^4T_2$ and $^4T_1$ state, respectively. $E\left(^4A_2 \rightarrow {}^4T_1\right)$ and $E\left(^4A_2 \rightarrow {}^4T_2\right)$ represent the spectral position of

$^4A_2 \rightarrow {}^4T_1$ and $^4A_2 \rightarrow {}^4T_2$ excitation bands. The energy position $E\left({}^4T_2\right)$ is determined by subtracting the relaxation energy $\Delta S/2$ from the spectral position of the $^4A_2 \rightarrow {}^4T_2$ excitation band. Herein, the relaxation energy is supposed to be the same for $^4A_2 \rightarrow {}^4T_1$ and $^4A_2 \rightarrow {}^4T_2$ transitions.

Table S8 The performance comparison between this work and previously reported near-infrared luminescent materials.

Sample	λ_{max} (nm)	IQE (%)	AE (%)	EQE (%)	Thermal stability	Device performance (@100 mA)	Ref
$Na_{1.4}Al_{0.3}Ti_{1.6}(PO_4)_3$:0.1Cr3+	831	51.7	46.6	24.1	50.2% @373 K	19.5 mW 6.83%	2
$LiMg_6AlO_8$:0.15Cr^{3+}	830	92.0	32.0	29.4	83% @423 K	48.2 mW 15.7%	5
$Li_{1.6}Mg_{1.6}Sn_{2.8}O_8$:0.06Cr^{3+}	860	51.6	59.5	30.7	46.5% @383K	25.2 mW 10%	6
$LiScP_2O_7$:0.06Cr^{3+}	880	38.0	52.6	20.0	23% @383 K	19 mW 7%	7
$CdTi_4(PO_4)_6$:0.09Cr^{3+}	832	46.6	49.2	22.9	58.6% @373 K	14.4 mW 5.5%	8
$Mg_4Sb_2O_9$:0.08Cr^{3+}	855	59.1	48.3	28.5	61.5% @373 K	17 mW 6%	9
$LiAlP_2O_7$:0.08Cr^{3+}	844	26.7	64.0	17.1	56% @373 K	9.7 mW 3.3%	10
$MgTiO_3$:0.005Cr^{3+}, 0.045In^{3+}	855	63.9	59.2	37.9	42.6% @373 K	28.2 mW 10.2%	This work

References:

1 M. Shi, Q. Shao, L. Yao, S. Yu, Y. Dong and J. Jiang, *Inorg. Chem.*, 2022, **61**, 12275-12283.

2 B. Yan, C. Wang, J. Wen, M. Zhu, Z. Xia, J. Ye, Q. Wang, X. Huang and L. Ning, *Mater. Today Chem.*, 2025, **47**, 102890.

3 L. Yao, Q. Jia, S. Yu, C. Liang and J. Jiang, Q. Shao, *Adv. Opt. Mater.*, 2023, **11**, 2202458.

4 G. Wang, T. Wang, Y. Yue, L. Hou, W. Huang, X. Zhu, H. Liu and X. Yu, *Laser Photonics Rev.*, 2024, **18**, 2400793.

5 Y. Yan, F. Huang, G. Zhu, S. Zhao, S. Ma, F. Huang, D. Deng and S. Xu, *Ceram. Int.*, 2026, **52**, 6805-6813.

6 X. Zhang, D. Sun, P. Luo, L. Zhou, X. Ye and H. You, *J. Mater. Chem. C*, 2024, **12**, 16422-16430.

7 L. Yao, Q. Shao, S. Han, C. Liang, J. He and J. Jiang, *Chem. Mater.*, 2020, **32**, 2430-2439.

8 B. Yan, J. Wen, Y. Zhou, S. Zhao, Q. Sha, X. Huang, Z. Dong, C.Wang, Q. Wang, L. Ning and C.-K. Duan, *Ceram. Int.*, 2025, **51**, 11018-11025.

9 J. Zhang, W. Zhao, Y. Li and J. Zhong, *J. Lumin.*, 2024, **266**, 120291.

10 L. Chen, J. Zhong, L. Zeng and W. Zhao, *J. Lumin.*, 2023, **263**, 120139.